IOP Conference Series: Materials
Science and Engineering

PAPER • OPEN ACCESS

Numerical study on the formation of spurious grains and freckles during the directional solidification of superalloys

To cite this article: H Zhang *et al* 2023 *IOP Conf. Ser.: Mater. Sci. Eng.* **1281** 012059

IOP Conf. Series: Materials Science and Engineering 1281 (2023) 012059 doi:10.1088/1757-899X/1281/1/012059

Numerical study on the formation of spurious grains and freckles during the directional solidification of superalloys

H Zhang[1], M Wu[1,*], X Liu[2,3], D Ma[2,3], M Song[2], A Ludwig[1], A Kharicha[1]

[1] Chair for Simulation and Modelling of Metallurgy Processes, Department of Metallurgy, University of Leoben, A-8700 Leoben, Austria
[2] State Key Laboratory of Powder Metallurgy, Central South University, Changsha 410083, China
[3] Wedge Central South Research Institute, Shenzhen 518045, China

E-mail: menghuai.wu@unileoben.ac.at

Abstract. Freckles, a significant issue encountered during the directional solidification of superalloys, are recognised by a trail of equiaxed grains parallel to the direction of gravity accompanied by local eutectic enrichment. In the current study, a mixed-columnar-equiaxed multiphase volume-average solidification model was employed to study the formation of freckles in superalloy casting. Fragments produced via flow-driven and capillary-driven fragmentation mechanisms are considered as the source of spurious grains. The transport and the growth/remelting of the fragments are considered. According to the simulation results, some segregation channels develop at the corners of the casting. Flow-driven fragments are produced in/around the segregation channels, whereas capillary-driven fragments are produced at a certain depth of the mushy zone across the entire section of the casting. The fragmentation rate caused by the flow-driven mechanism is several orders of magnitude larger than that caused by the capillary-driven mechanism, i.e. the flow-driven fragmentation mechanism is dominant for the currently investigated sample. After the solidification process, four freckles formed at the casting corners on the shadowed side, whereas it was freckle-free on the bright side.

1. Introduction

Single-crystal superalloy turbine blades fabricated using directional solidification (DS) are key components of aeroengines and gas turbines. Such components are susceptible to flow-induced freckle defects, which are recognised by a trail of spurious/stray grains parallel to the direction of gravity, accompanied by the local enrichment of eutectics [1]. The freckling mechanism is well-understood experimentally. The thermo-solutal convection due to the liquid density inversion in the mushy zone is responsible for the onset of freckles [2,3]. The segregation of the alloying elements makes the interdendritic liquid less dense than the bulk liquid. In the event of an upward DS, the light interdendritic liquid tends to flow upward to release its gravitational potential, and thereby, some plumes form at the solidification front. After merging and competing with each other, only a few plumes survive and further develop into stable segregation channels. The solute-enriched liquid is continuously sucked into the channel. The roots of higher-order sidearms can be remelted by flow-induced solute enrichment or capillary effects [4,5], that is, dendrite fragmentation occurs.

Near the open mouth of the segregation channel, small fragments are transported out of the mushy zone by upwelling (upward flow of solute-enriched liquid enclosed in the plume) and finally remelted in the top hot liquid [6]. Deep in the mushy zone, the fragments sink and continue to grow into spurious grains [2], and the residual solute-enriched liquid solidifies as eutectics. The formation of the freckle is a consequence of a long and complex process involving the aforementioned solidification physics. The quantitative prediction of such a freckling process through an experimental study is still not feasible. Alternatively, numerical modelling has gradually made it possible to visualise the casting process and accurately predict the formation of freckles. According to state-of-the-art simulations [7–10], the freckles were indirectly predicted through the calculated segregation channels. The significant role of the fragments, which are the main source of the spurious grains, was ignored or roughly treated [11].

In this study, a three-phase mixed columnar-equiaxed solidification model [12] was used to simulate the DS of superalloy casting. The model was recently extended to consider flow- and capillary-driven fragmentation mechanisms [5]. The remelting and solidification of the as-formed solid phases (i.e. columnar dendrites and equiaxed grains) were also considered [13]. The main goal of this study was to numerically investigate the formation of spurious grains produced by different fragmentation mechanisms, and hence the onset of freckles.

2. Model configuration and calculation method

A cluster of Ni-based superalloy specimens was directionally solidified in a Bridgman-type vacuum furnace. The shell mould produced by the normal investment casting procedure was placed on a copper-chill base. A typical spiral grain selector, including the starter block, was used to realise the single-crystal solidification of the casting. The shell mould was preheated first, and then the hot melt was poured into the mould. The solidification of the casting was triggered by withdrawing the sample downwards from the heated zone to the cold zone at a constant velocity of 3 mm/min. The composition of the superalloy is listed in Table I. After the casting process, the superalloy casting was knocked out from the shell mould and mechanically separated from the casting cluster, followed by metallographic analysis.

Table I. Main composition of the considered superalloy.

Elements	Ni	Ta	Cr	Al	Co	W	Re	Ti	Mo
Content (wt.%)	-	8.07	3.39	5.69	5.97	6.52	4.89	0.15	0.41

A full-scale geometry of the Bridgman furnace and casting system was constructed for the current simulation. As shown in Figure 1(a), only a sector of 30º of the furnace containing one casting was considered. The dimensions of the casting are shown in Figures 1(b) and (c). The DS process was simulated in two steps. The first step is to calculate the global thermal field in the Bridgman furnace, including the casting system, and the second step is to calculate the flow and solidification in the casting. The former was performed using the commercial software ProCAST, whereas the latter was performed using our previously developed multiphase volume-average-based (VA) solidification model. The thermal calculation was based on the full-scale geometry (Figure 1(a)), and the flow-solidification calculation was restricted to the casting body (Figure 1(b)).

For the thermal calculation in ProCAST, the top hot and bottom cold chambers were set to fixed temperatures of 1773 K and 353 K, respectively. The radiation was considered between the inducting wall and shell mould, and the withdrawing process was realised by raising the furnace. The calculation started from a mould fully filled with the superalloy melt, i.e. the filling process was ignored. The conservation of enthalpy was solved for the shell mould and casting, but only latent heat owing to solidification of the casting was treated with an equivalent specific heat method [10].

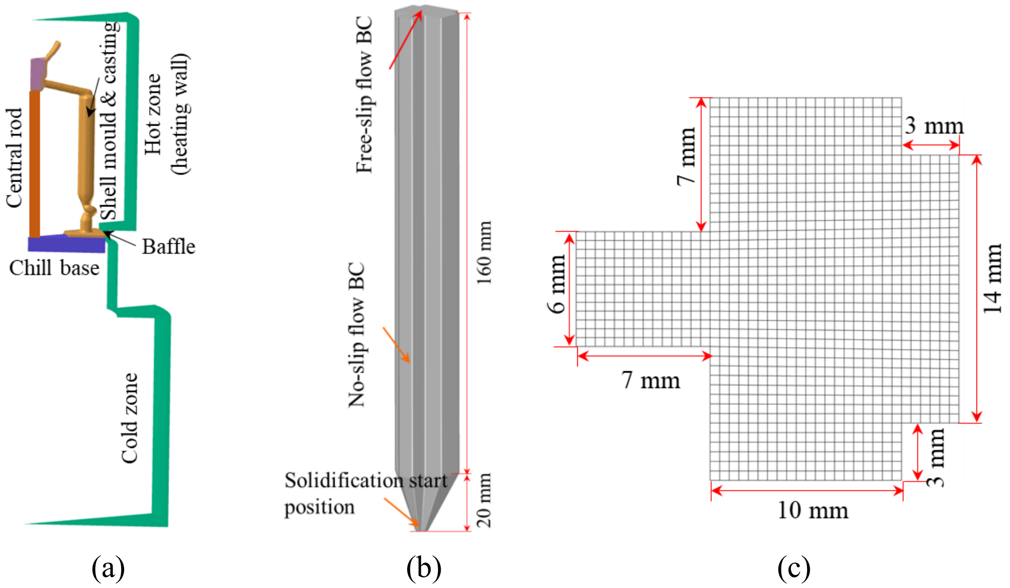

Figure 1. (a) Layout of the Bridgman furnace and the casting system; (b) shape of the sample casting; (c) dimension of the casting.

Flow and solidification were solved using the VA multiphase solidification model. Three hydrodynamic phases were involved: the liquid melt, equiaxed grains, and columnar dendrites with volume fractions of up to one ($f_\ell + f_e + f_c = 1$). The morphology of the columnar dendrites was approximated by growing cylinders. The equiaxed dendrites were simplified as spheres. Thermodynamic equilibrium was assumed at the solid–liquid interface. Diffusion-governed growth kinetics was considered to calculate the solidification/remelting rate. The concentration difference between the thermodynamic equilibrium concentration of the liquid at the interface (c_ℓ^*) and the volume-averaged liquid concentration (c_ℓ) served as the driving force for solidification and remelting. The columnar structure was initiated only from the bottom of the casting, and its tip front was traced using the Lipton–Glicksman–Kurz (LGK) model [14]. In the current study, equiaxed grains were assumed to originate from dendrite fragmentation, and two fragmentation mechanisms, i.e. capillary- and flow-driven fragmentation mechanisms, were considered. Remelting and destruction of the equiaxed grains were also considered. The conservation of the number density of the equiaxed grains was solved considering the transport of equiaxed grains:

$$\frac{\partial}{\partial t} n_e + \nabla \cdot \left(\vec{u}_e n_e \right) = N_{\mathrm{frag}}^{\mathrm{capillary}} + N_{\mathrm{frag}}^{\mathrm{flow}} + N_{\mathrm{des}} , \qquad (1)$$

where n_e and $\vec{u}_e$ are the number density and velocity of the equiaxed grains; $N_{\mathrm{frag}}^{\mathrm{capillary}}$ and $N_{\mathrm{frag}}^{\mathrm{flow}}$ are the fragmentation rates due to capillary- and flow-driven mechanisms; and N_{des} is the destruction rate of the grains through remelting. The formulations for these terms and the meanings of the relevant symbols are summarised in Table II.

The production rate of fragments via the capillary-driven mechanism ($N_{\mathrm{frag}}^{\mathrm{capillary}}$) was calculated based on equation (2) [15,16], in which a is an alloy-dependent constant, and S_V is the interfacial area density. A general expression for S_V was shown in equation (3) [17], which accounted for the effects of dendrite growth, coarsening, and interface coalescence. The initial size of the formed fragments ($d_{\mathrm{e,frag}}^0$) was assumed to be inversely proportional to S_V, equation (4) [18]. Since a spherical morphology was assumed for the equiaxed grains, the corresponding mass transfer rate ($M_{\text{frag}}^{\text{capillary}}$) from the columnar to the equiaxed due to the capillary-driven fragmentation can be calculated by equation (5) [16].

Table II. Formulations for $N_{\text{frag}}^{\text{capillary}}$, $N_{\text{frag}}^{\text{flow}}$, and N_{des}

Terms	Equations	Symbols	Refs.
$N_{\text{frag}}^{\text{capillary}}$	**Capillary-driven fragmentation:** $N_{\text{frag}}^{\text{capillary}} = \frac{\mathrm{d}\left(a \cdot S_V{}^3\right)}{\mathrm{d}t}$ (2) $S_V = f_c (1-f_c)^{\tilde{r}} \left(\left(S_{S0}{}^{-1}\right)^3 + K_0 t_s\right)^{-1/3}$ (3) $d_{\text{e,frag}}^0 = f_c \frac{1.6}{S_V}$ (4) $M_{\text{frag}}^{\text{capillary}} = N_{\text{frag}}^{\text{capillary}} \left(\rho_e \frac{\pi}{6}\left(d_{\text{e,frag}}^0\right)^3\right)$ (5)	S_V: interfacial area density a, $\tilde{r}$, S_{S0}, K_0: alloy-dependent constants f_c: volume fraction of columnar phase $d_{\text{e,frag}}^0$: initial size of the fragment $M_{\text{frag}}^{\text{capillary}}$: mass transfer rate from columnar to equiaxed due to capillary-driven fragmentation ρ_e: equiaxed density	[15,16,18]
	$a = 1.0\times10^{-5}$, $\tilde{r} = 0.4$, $S_{S0}{}^{-1} = 246.0$ μm, $K_0 = 23.5$ μm^3/s, $\rho_e = 7646.0$ kg/m^3		
$N_{\text{frag}}^{\text{flow}}$	**Flow-driven fragmentation:** $M_{\text{frag}}^{\text{flow}} = -\gamma \cdot (\vec{u}_\ell - \vec{u}_c) \cdot \nabla c_\ell \cdot \rho_e \cdot f_c$ (6) $N_{\text{frag}}^{\text{flow}} = \frac{M_{\text{frag}}^{\text{flow}}}{\frac{\pi}{6}\left(d_{\text{e,frag}}^0\right)^3 \rho_e}$ (7)	$M_{\text{frag}}^{\text{flow}}$: mass transfer rate from columnar to equiaxed due to flow-driven fragmentation γ: fragmentation coefficient $\vec{u}_\ell$: liquid velocity $\vec{u}_c$: columnar velocity ∇c_ℓ: liquid concentration gradient	[5,19]
	$\gamma = 2.0\times10^{-5}$		
N_{des}	**Grain destruction:** $\frac{\mathrm{d}n_e}{\mathrm{d}x} = \frac{n_e}{\sqrt{2\pi}\sigma_d x} e^{-\frac{1}{2}\left(\frac{\ln(x)-\ln(\hat{d}_e)}{\sigma_d}\right)^2}$ (8) $N_{\text{des}} = v_{\text{Re}} \cdot \left.\frac{d(n_e)}{d(x)}\right\|_{x=d_{\text{e,critical}}}$ (9) $v_{\text{Re}} = \frac{D_\ell}{l_\ell} \cdot \frac{\left(c_\ell^* - c_\ell\right)}{(1-k)c_\ell^*}$ (10)	x: grain diameter of various size classes v_{Re}: grain remelting speed σ_d: geometric standard deviation $\hat{d}_e$: geometric mean of the grain diameter D_ℓ: liquid diffusion coefficient l_ℓ: liquid diffusion length c_ℓ^*: equilibrium liquid concentration c_ℓ: volume-averaged liquid concentration k: solute partition coefficient	[5,13]
	$\sigma_d = 0.873$, $d_{\text{e,critical}} = 50$ μm, $D_\ell = 3.6\times10^{-9}$ m^2/s, $k = 0.569$		

Based on the fact that a flow in the growth direction of primary columnar dendrites in the mushy zone promotes re-melting, the mass transfer rate ($M_{\text{frag}}^{\text{flow}}$) from the columnar to the equiaxed due to the flow-induced fragmentation was assumed to be proportional to the value of $-(\vec{u}_\ell - \vec{u}_c)\cdot\nabla c_\ell$, equation (6) [19]. The fragmentation coefficient γ is to bridge all other unknown contributors to $M_{\text{frag}}^{\text{flow}}$. Because of the assumed spherical morphology for the equiaxed grains, the production rate of flow-driven fragments can be calculated via equation (7). Refer to equation (4) for the initial size of the fragments.

The equiaxed grains, and the newly produced fragments, shall be remelted and destroyed if they are exposed to a hot liquid. Because the grain remelting was assumed to be governed by diffusion, equation (10) was valid to calculate the remelting speed v_{Re}. In each calculation cell, the equiaxed grains were assumed to follow a lognormal size distribution, equation (8) [13]. When the grain diameter was melted to smaller than a critical value $d_{e,critical}$, the grain would be eliminated from the casting domain, i.e. grain destruction occurred. The destruction rate of the equiaxed grains was calculated via equation (9). More fundamentals of the VA multiphase solidification model have been detailed in [12].

The cooling history of the temperature distribution on the casting surface, as calculated by ProCAST, was used as the Dirichlet thermal boundary condition for the flow-solidification calculation using VA solidification model. The thermal coupling method has been introduced in [10]. As shown in Figure 1(b), a no-slip flow boundary condition was applied to the lateral wall of the sample, and a free-slip flow boundary condition was applied to the top surface. The alloy was assumed to be incompressible, with constant density and viscosity.

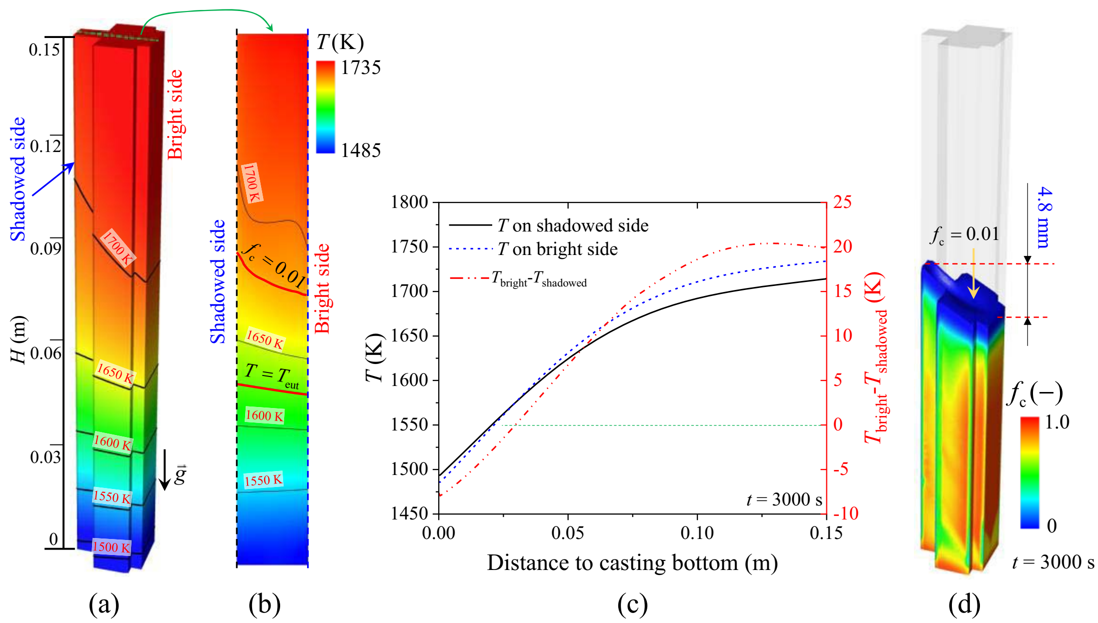

Figure 2. Analysis of the calculated temperature (T) in the casting. (a)-(b) T field on the casting surface and casting vertical section. (c) T profiles along the two vertical dashed lines in (b), and the temperature difference between the two lines. (d) Calculated volume fraction of the columnar phase f_c, and the shape of the solidification front ($f_c = 0.01$).

3. Interpretation of simulation results

3.1. Temperature field

The calculated temperature on the casting surface at $t = 3000$ s is shown in Figure 2(a). The bottom of the sample is 250 K cooler than the top. Owing to the shadow effect in the furnace, the shadowed side facing the central rod is cooler than the bright side facing the inducting wall. The temperature on the central vertical

IOP Conf. Series: Materials Science and Engineering 1281 (2023) 012059 doi:10.1088/1757-899X/1281/1/012059

section of the casting is presented in Figure 2(b), where the solidification front (f_c = 0.01) and eutectic isotherm ($T = T_{eut}$) are marked. The isotherms (e.g. T = 1700 K) are bent by the liquid convection in the top liquid region. The temperature profiles along the two dashed lines in Figure 2(b) are plotted in Figure 2(c), and the temperature difference between the two lines ($T_{bright} - T_{shadowed}$) is also overlaid. From the top to the bottom of the sample, the temperature difference changes from positive to negative gradually. In the top part of the sample, the temperature on the bright side is 20 K higher than that on the shadowed side. Owing to this temperature difference, the solidification front is significantly inclined. According to the current simulation results shown in Figure 2(d), the solidification front on the shadowed side is 4.8 mm higher than that on the bright side.

3.2. Liquid flow pattern

Typical solidification results at t = 2500 s are shown in Figure 3. Figure 3(a) presents the contour of the columnar fraction (f_c) and the shape of the solidification front. The liquid flow of the top hot liquid is overlaid on the vertical section. Figure 3(b) depicts the liquid concentration (c_ℓ) on the casting surface, on which the isolines for f_c=0.01 and T=T_{eut} are drawn. The liquid density (ρ_ℓ) is shown in Figure 3(c). The liquid flow in the plumes and freckles is depicted in Figure 3(d). It should be addressed that ρ_ℓ is a post-processed result according to local T and c_ℓ, i.e. $\rho_\ell = \rho_\ell^{ref} \cdot \left(1 + \beta_T \cdot \left(T - T^{ref}\right) + \beta_c \cdot \left(c_\ell - c^{ref}\right)\right)$, in which ρ_ℓ^{ref}, T^{ref}, and c^{ref} are the reference density, temperature, and liquid concentration; β_T and β_c are the thermal and solutal expansion coefficients.

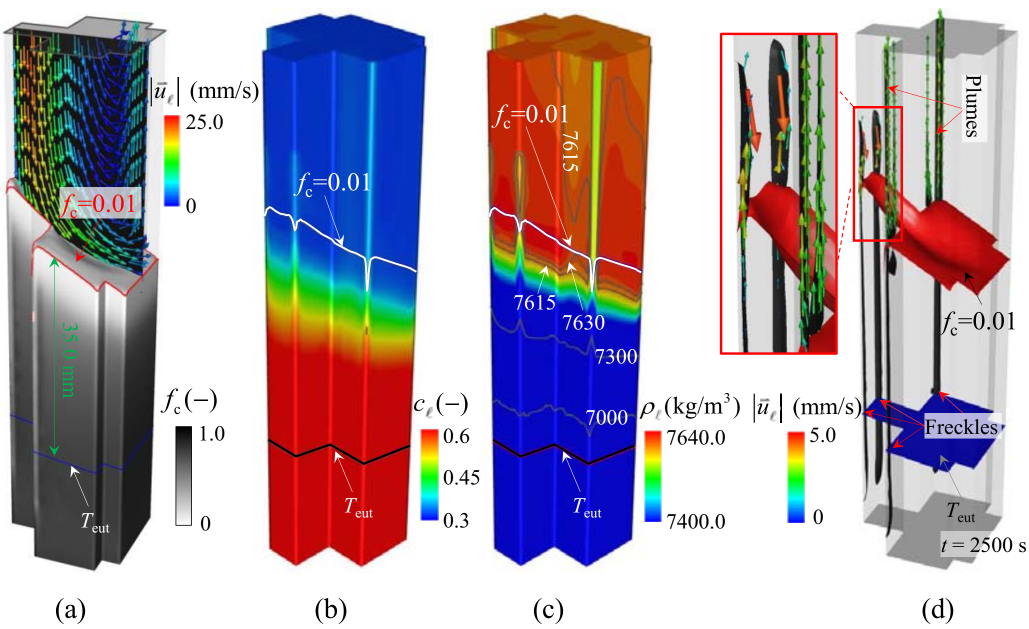

Figure 3. Typical solidification results at t = 2500 s. (a) Contour of the volume fraction of columnar phase f_c. The liquid convection of the top hot liquid is shown by the colourful vectors on the vertical section. (b) Contour of the liquid concentration c_ℓ. (c) Contour of the liquid density ρ_ℓ. (d) Iso-surfaces in black are to show the distribution of the plumes and freckles. The fluid flow in the plumes and freckles is shown by the vectors.

Because of the horizontal temperature gradient, the melt flows downwards on the shadowed side and then flows upwards on the bright side, Figure 3(a). Under the current cooling condition, a 35 mm thick mushy zone developed. In the mushy zone, the solute was rejected from the solid to the liquid owing to the alloy solidification. As shown in Figure 3(b), c_ℓ increases with the depth of the mushy zone. Because $\rho_\ell = \rho_\ell^{\text{ref}} \cdot \left(1 + \beta_{\text{T}} \cdot \left(T - T^{\text{ref}}\right) + \beta_{\text{c}} \cdot \left(c_\ell - c^{\text{ref}}\right)\right)$, as depicted in Figure 3(c), above the solidification front, ρ_ℓ decreases with the height of the casting owing to the increased temperature; below the solidification front, ρ_ℓ decreases with the depth of the mush owing to the solute enrichment; and the maximal $\rho_\ell\left(7630\ \text{kg/m}^3\right)$ is found near the solidification front. The inversion of ρ_ℓ makes the liquid hydrodynamically unstable. The solute-enriched liquid in the mushy zone tends to flow upward owing to its low density, which leads to the onset of the plumes. As depicted in Figure 3(d), some plumes develop on the shadowed side, and the light solute-enriched liquid flows upward along the plumes. The vertical transport of the solute-enriched liquid raises c_ℓ in and near the plumes (Figure 3(b)), and thereby drops ρ_ℓ locally (Figure 3(c)).

Note that plumes only formed on the shadowed (left) side of the casting. The onset of plumes is highly related to the shape of the solidification front. At the peak of the inclined solidification front, the solute-enriched interdendritic liquid exhibited the highest gravitational potential energy to flow upwards, making it the preferred position for the formation of the plumes. This has been theorised in our previous work [10]. As shown in Figure 3(d), four plumes located as the casting corners further developed into stable freckles below the solidification front. On the bright (right) side, it is free of plumes and freckles.

3.3. Formation of spurious grains via different fragmentation mechanisms

Two fragmentation mechanisms, i.e. flow- and capillary-driven mechanisms, have been considered in the current study, and the calculated $N_{\text{frag}}^{\text{flow}}$ and $N_{\text{frag}}^{\text{capillary}}$ are depicted in Figures 4(a) and (b), respectively. The flow-driven fragments are produced near the solidification front and around the segregation channels, but the capillary-driven fragments are generated at a distance below the solidification front. Additionally, the capillary-driven fragmentation occurs throughout the whole sample cross-section except the freckled areas. The production efficiency of the two fragmentation mechanisms is also quite different. According to the current simulation results, $N_{\text{frag,max}}^{\text{flow}}$ = 7.5×10^8 (m^{-3}·s^{-1}), whereas $N_{\text{frag,max}}^{\text{capillary}} = 1073\ \text{m}^{-3} \cdot \text{s}^{-1}$. Different from the results of $N_{\text{frag}}^{\text{flow}}$, a negative value of $N_{\text{frag}}^{\text{capillary}}$ is predicted in the lower part of the mushy zone (Figure 4(b)), which indicates that some fragments vanished because of dendrite coarsening (coalescence or remelting) [5].

4. Discussions

The freckles are recognised by a trail of equiaxed (spurious) grains parallel to the direction of gravity, and the dendrite fragmentation is believed to be the main source for the equiaxed grains [2,4]. According to state-of-the-art simulations [7–10], due to the lack of a reliable fragmentation model, the freckles were indirectly predicted through the calculated segregation channels by ignoring the formation of equiaxed grains. In this study, the formation of equiaxed grains via two different fragmentation mechanisms [5,15,19] are numerically investigated. The calculation of flow and solidification in the superalloy casting was coupled with radiation in the Bridgman furnace.

As shown in the inset of Figure 3(d), the liquid in the freckles beneath the solidification front flows upward. Despite the low flow strength, some fragments created near the open mouths of the freckles were transported out of the mushy zone into the top hot liquid. The remelting and grain destruction occurred subsequently. Remelting of the equiaxed grains also happened in the freckled areas owing to the increase in

IOP Publishing
doi:10.1088/1757-899X/1281/1/012059

liquid concentration. The rest of the formed fragments sedimented in the freckles and continued to solidify. These fragments blocked the horizontal growth of columnar dendrites toward the freckles. After the solidification process, the fragments grew into coarse spurious grains, and the residual liquid solidified as eutectics.

Comparing Figures 4(a) and (b), in addition to the flow-driven fragments in/around the segregation channels, a small number of capillary-driven fragments were generated deep in the mushy zone. Since columnar dendrites were fully developed there, the capillary-driven fragments could hardly be transported. Their growth was also suppressed by the as-developed columnar dendrites. Based on the current numerical study, in the main body of the casting, the casting was dominated by a columnar structure ($f_c \approx 0.9$) with a small amount of eutectics ($f_{eut} \approx 0.1$). In the freckled areas, the sum of the volume fractions of the equiaxed grains and eutectics is up to 0.75, whereas $f_c < 0.25$. Such simulation results are consistent with our experimental observations. Further analysis of the simulation results and a quantitative comparison between the simulation and the experiment will be presented in the following journal paper.

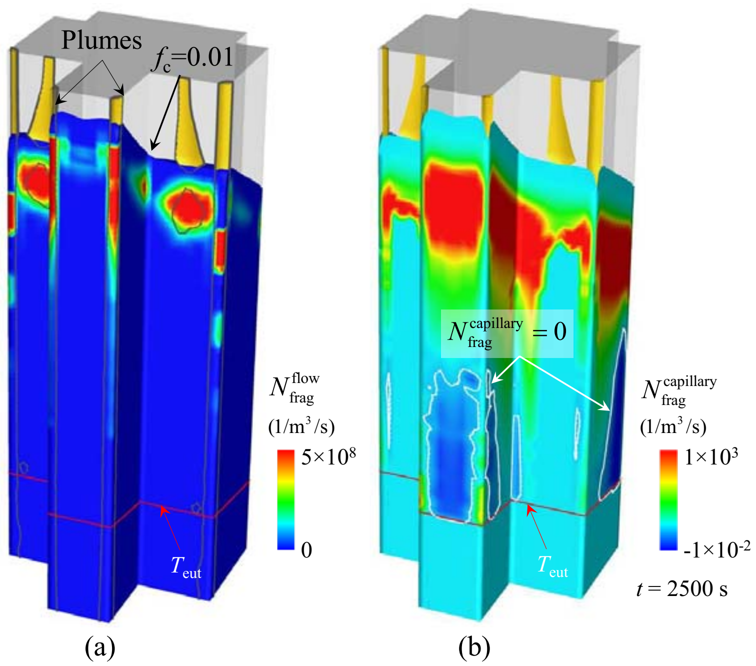

Figure 4. Analysis of the formation of spurious grains via dendrite fragmentation. The yellow shapes on the top indicate the as-developed plumes. (a) Contour of the flow-driven fragmentation rate N_{frag}^{flow}. (b) Contour of the capillary-driven fragmentation rate $N_{frag}^{capillary}$. The isoline for $N_{frag}^{capillary} = 0$ is overlaid. $N_{frag}^{capillary}$ is negative inside the white line and positive outside the white line.

5. Conclusions

The formation of spurious grains and freckles during directional solidification of superalloys was numerically studied using a mixed-columnar-equiaxed volume-average solidification model. Two different fragmentation mechanisms, i.e. capillary-driven and flow-driven fragmentation mechanisms, were considered to produce spurious grains. The following conclusions were drawn for the currently studied sample:

1) Flow-driven fragmentation primarily occurred in/around the segregation channels, whereas capillary-driven fragmentation occurred throughout the entire cross-section of the casting, except in the segregation channel areas.

2) The fragmentation rate caused by the flow-driven mechanism was several orders of magnitude larger than that of the capillary-driven mechanism. The flow-driven fragmentation mechanism contributed mostly to the formation of spurious grains in the freckles.

3) Owing to the shadow effect of the Bridgman furnace, the shadowed side of the casting could be 20 K cooler than the bright side. Thus, the solidification front was significantly inclined. Plumes only formed on the shadowed side, and four plumes developed further into freckles at the casting corners. On the bright side, it was free of plumes and freckles.

6. Acknowledgements

This work was financially supported by the Austrian Science Fund in the framework of the FWF-NKFIN joint project (FWF, I4278-N36).

References

[1] Giamei A F and Kear B H 1970 On the nature of freckles in nickel base superalloys *Metall. Trans.* **1** 2185–92
[2] Hellawell A, Sarazin J R and Steube R S 1993 Channel convection in partly solidified systems *Philos. Trans. - R. Soc. London, A* **345** 507–44
[3] Auburtin P, Wang T, Cockcroft S L and Mitchell A 2000 Freckle formation and freckle criterion in superalloy castings *Metall. Mater. Trans. B* **31** 801–11
[4] Copley S M, Giamei A F, Johnson S M and Hornbecker M F 1970 The origin of freckles in unidirectionally solidified castings *Metall. Trans.* **1** 2193–204
[5] Zhang H, Wu M, Rodrigues C M G, Ludwig A, Kharicha A, Rónaföldi A, Roósz A, Veres Z and Svéda M 2022 Dendrite fragmentation mechanism under forced convection condition by rotating magnetic field during unidirectional solidification of AlSi7 alloy *Acta Mater.* 118391
[6] Hellawell A, Liu S and Lu S Z 1997 Dendrite fragmentation and the effects of fluid flow in castings *Jom* **49** 18–20
[7] Schneider M C, Gu J P, Beckermann C, Boettinger W J and Kattner U R 1997 Modeling of micro- and macrosegregation and freckle formation in single-crystal nickel-base superalloy directional solidification *Metall. Mater. Trans. A* **28** 1517–31
[8] Felicelli S D, Heinrich J C and Poirier D R 1998 Three-dimensional simulations of freckles in binary alloys *J. Cryst. Growth* **191** 879–88
[9] Wu M, Stefan-Kharicha M, Kharicha A and Ludwig A 2021 Flow-solidification interaction: A numerical study on solidification of NH4Cl – 70 wt.%H2O solution in a water-cooled mould with a large sample thickness *Int. J. Heat Mass Transf.* **164** 120566
[10] Zhang H, Liu X, Ma D, Song M, Ludwig A, Kharicha A and Wu M 2023 Digital twin for directional solidification of a single-crystal turbine blade *Acta Mater.* **244** 118579
[11] Gu J P, Beckermann C and Giamei A F 1997 Motion and remelting of dendrite fragments during directional solidification of a nickel-base superalloy *Metall. Mater. Trans. A Phys. Metall. Mater. Sci.* **28** 1533–42
[12] Wu M and Ludwig A 2006 A three-phase model for mixed columnar-equiaxed solidification *Metall. Mater. Trans. A* **37** 1613–31
[13] Zhang H, Wu M, Schumacher P, Rodrigues C M G, Ludwig A and Kharicha A 2021 Modelling melting and grain destruction phenomena during globular equiaxed solidification *Appl. Math. Model.* **97** 821–38
[14] Lipton J, Glicksman M E and Kurz W 1987 Equiaxed dendrite growth in alloys at small supercooling *Metall. Trans. A* **18** 341–5
[15] Cool T and Voorhees P W 2017 The evolution of dendrites during coarsening: Fragmentation and morphology *Acta Mater.* **127** 359–67
[16] Rodrigues C M G, Wu M, Zhang H, Ludwig A and Kharicha A 2021 Bridging Capillary-Driven

Fragmentation and Grain Transport with Mixed Columnar-Equiaxed Solidification *Metall. Mater. Trans. A* **52** 4609–22
[17] Neumann-Heyme H, Eckert K and Beckermann C 2017 General evolution equation for the specific interface area of dendrites during alloy solidification *Acta Mater.* **140** 87–96
[18] Li Q and Beckermann C 1998 Scaling behavior of three-dimensional dendrites *Phys. Rev. E* **57** 3176–88
[19] Zheng Y, Wu M, Kharicha A and Ludwig A 2018 Incorporation of fragmentation into a volume average solidification model *Model. Simul. Mater. Sci. Eng.* **26** 015004